

# The Neutron Halo in Heavy Nuclei Calculated with the Gogny Force\*

B. Nerlo-Pomorska and K. Pomorski

*Theoretical Physics Department, Maria Curie-Skłodowska University  
ul. Radziszewskiego 10, 20-031 Lublin, Poland*

J. F. Berger and J. Dechargé

*Commissariat à l'Energie Atomique, Service de Physique Nucléaire  
B.P. 12, 91680 Bruyères-le-Châtel, France*

## Abstract

The proton and neutron density distributions, one- and two-neutron separation energies and radii of nuclei for which neutron halos are experimentally observed, are calculated using the self-consistent Hartree-Fock-Bogoliubov method with the effective interaction of Gogny. Halo factors are evaluated assuming hydrogen-like antiproton wave functions. The factors agree well with experimental data. They are close to those obtained with Skyrme forces and with the relativistic mean field approach.

## 1 Introduction

In the last years, more and more experimental evidence concerning neutron distributions in nuclei has become available [1]. In particular, it has been found that several neutron rich nuclei display a neutron skin or even a neutron ‘stratosphere’ called the neutron halo. Such properties of neutron distributions have been predicted by the asymptotic density model [2], the relativistic mean field theory [3], and Hartree-Fock calculations with Skyrme forces [1].

With the increasing amount of experimental data available, halo factors can now be used as an additional test of nuclear effective interactions. Namely, microscopic approaches should be able to reproduce not only binding energies and charge radii, but also the detail of density distributions, especially density tails at large distance from the nucleus center.

---

\*The work is partly supported by the Polish Committee of Scientific Research under Contract No. 2P03B 011 12

The aim of this work is to perform such a test for the effective interaction proposed by Gogny [4]. While many applications have shown the high quality of this force for describing a wide range of nuclear properties [4–7], no systematic study in this direction has been made up to now. The mean-field theory employed with the Gogny force is applied to nineteen halo nuclei found in [1]. We calculate neutron and proton density distributions at large distance, one- and two-neutron separation energies, and the halo factors related to the probability of annihilation of antiproton from atomic-like orbitals. These results are compared with experimental data and with Hartree-Fock calculations performed with the SLy4 interaction [8].

In Section 2, we recall the form of the Gogny effective interaction and we describe the method by which the results mentioned above are obtained numerically. In Section 3, neutron separation energies and density distributions at large distance from the center of the nucleus are analyzed. In Section 4, the prescription employed for evaluating halo factors is given and the theoretical values obtained are compared with experimental data. Conclusions and plans for further investigations are presented at the end of the paper.

## 2 Description of the approach

The Gogny two-body effective nuclear interaction has the following form [4] :

$$\begin{aligned}
V_{12} = & \sum_{i=1}^2 \exp \left[ -\frac{|\vec{r}_1 - \vec{r}_2|^2}{\mu_i^2} \right] \cdot (W_i + B_i \hat{P}_\sigma - H_i \hat{P}_\tau - M_i \hat{P}_\sigma \hat{P}_\tau) + \\
& + t_3 (1 + x_0 \hat{P}_\sigma) \delta(\vec{r}_1 - \vec{r}_2) \left[ \rho \left( \frac{\vec{r}_1 + \vec{r}_2}{2} \right) \right]^\gamma + \\
& + i W_{LS} (\vec{\sigma}_1 + \vec{\sigma}_2) \cdot \vec{\nabla}_{12} \times \delta(\vec{r}_1 - \vec{r}_2) \vec{\nabla}_{12} + V_{\text{Coul.}} ,
\end{aligned} \tag{1}$$

The first line represents two finite range terms ( $i = 1, 2$ ), with the usual superposition of Wigner, Bartlett, Heisenberg and Majorana spin-isospin contributions.  $\vec{r}_i$  is the space coordinate of nucleon  $i$ , and  $\hat{P}_\sigma$  and  $\hat{P}_\tau$  are the exchange operators of spin and isospin variables, respectively. The second line of eq. (1) describes a two-body zero-range density-dependent interaction. The last line contains a two-body zero-range spin-orbit term and the Coulomb potential between protons. Here,  $\vec{\nabla}_{12} = \vec{\nabla}_1 - \vec{\nabla}_2$ , and  $\vec{\sigma}_i$  is twice the spin operator of nucleon  $i$ .

The set of parameters adopted since 1983, called D1S [7], is:

$\mu_1 = 0.7 \text{ fm}$	$\mu_2 = 1.2 \text{ fm}$
$W_1 = -1720.3 \text{ MeV}$	$W_2 = 103.639 \text{ MeV}$
$B_1 = 1300 \text{ MeV}$	$B_2 = -163.483 \text{ MeV}$
$H_1 = -1813.53 \text{ MeV}$	$H_2 = 162.812 \text{ MeV}$
$M_1 = 1397.60 \text{ MeV}$	$M_2 = -223.934 \text{ MeV}$
$t_3 = 1390.60 \text{ MeV fm}^{3(1+\gamma)}$	$x_0 = 1$
$\gamma = 1/3$	$W_{LS} = 130 \text{ MeV fm}^5$

Hartree-Fock-Bogoliubov (HFB) self-consistent calculations have been carried out with this interaction, with the purpose of extracting binding energies and nucleon density distributions. Similar results employing the Hartree-Fock (HF) method, i.e. ignoring pairing correlations, have also been derived in order to compare them with those obtained with the Skyrme HF method. All calculations have been performed in spherical symmetry. The method used is described in detail in Ref. [4]. The assumption of a spherical mean-field may seem inappropriate for those halo nuclei which ground states are deformed. However, since halo factors depend essentially on the slope of the density at very large distance from the nuclear surface, such a simplification should be sufficient for a first estimate of their magnitudes. In the same spirit, the effect on nuclear densities of correlations beyond the mean-field approximation, as those coming from oscillations around a fixed shape or from large amplitude collective vibrations [9, 10] has been ignored in the present study. One should nevertheless keep in mind that neglecting the increase of neutron and proton radii caused by deformation and correlations should lead to a slight underestimation of halo factors in most nuclei.

Our calculations are performed by expanding the HFB one quasi-particle states on finite harmonic oscillator (HO) bases. A crucial point in this method is to carefully choose the two parameters: number of shells ( $N_{MAX}$ ) and harmonic oscillator frequency  $\hbar\omega$ , on which these bases depend. This is especially needed in the present study where the behaviour of single-particle wave-functions at large distance from the center of the nucleus has to be accurately determined. The method we have employed consists of choosing, for each value of  $N_{MAX}$ , the  $\hbar\omega$  value that minimizes the HFB binding energy. Then  $N_{MAX}$  is increased until convergence of the HFB binding energy is obtained.

Application of this method to  $^{58}\text{Ni}$  is illustrated in Figs. 1, 2 and 3. Fig.1 displays the variations of the HFB energy ( $B$ ) with  $\hbar\omega$  for  $N_{MAX}=16$ . The energies of the minima of the curves  $B(\hbar\omega)$  are plotted in Fig.2 as functions of  $N_{MAX}$ . One observes that convergence of the HFB binding energy is obtained for  $N_{MAX}=16$  in this nucleus. As shown in Fig.3, a well defined energy minimum is then obtained in the  $(\hbar\omega, N)$  plane. This procedure has been employed for the nineteen halo-nuclei considered in the present study.

In order to illustrate the influence of the HO basis parameters on densities, we have plotted in Fig. 4 the logarithm of the neutron density distribution  $\log \rho_n$  of  $^{58}\text{Ni}$  versus the radial distance  $r$  for a few values of  $\hbar\omega$ . One can see that  $\rho_n$  is sensitive to the chosen  $\hbar\omega$  only in the peripheral region  $r > 8$  fm, a region where  $\rho_n$  is smaller than  $10^{-10}$  fm $^{-3}$ .

### 3 Results

The parameters of the HO bases employed for all the halo-nuclei studied in the present work are gathered in Table 1. The HO frequency  $\hbar\omega$  corresponding to the minimal HFB energy and the number of shells  $N_{MAX}$  above which the energy does not change any more are shown for each nucleus. The HFB energy and the one- and two-neutron separation energies  $S_n$  and  $S_{2n}$  are also listed. The separation energies have been found by subtraction

of the HFB energies of neighbouring isotopes

$$S_n(Z, N) = B(Z, N) - B(Z, N - 1) , \quad (2)$$

$$S_{2n}(Z, N) = B(Z, N) - B(Z, N - 2) , \quad (3)$$

Odd isotope energies have been calculated using the blocking version of the HFB theory, as described in Ref. [4]. In each nucleus, the blocked quasi-particle state has been chosen as the one having the experimentally known spin nearest to the neutron Fermi surface. Quadrupole deformations  $\beta_2$  taken from Ref. [11] are given in Table 1 in order to indicate which nuclei are deformed in their ground states. Let us recall that all nuclei are considered as spherical in our calculation. The last two columns of Table 1 display calculated and experimental halo factors, the meaning of which will be explained in Section 4.

The one- and two-neutron separation energies of these nuclei are compared with the experimental values [12] in Figs. 5 and 6. In these figures, the differences between experimental and theoretical separation energies are plotted as functions of the proton number  $Z$ .

Calculated neutron separation energies agree with experiment within  $\pm 1$  MeV in spherical nuclei, except for  $^{48}\text{Ca}$ ,  $^{96}\text{Ru}$ ,  $^{130}\text{Te}$  and  $^{144}\text{Sm}$ . In these nuclei, the neutron Fermi level is located in the vicinity of a major shell gap, where the single-particle level density is underestimated in the present mean-field approach. A proper description of separation energies in nuclei near closed shells would require to take into account correlations beyond the mean-field – as RPA ground state correlations – and the induced spectroscopic factors and single-particle level displacements. Let us also note that, in the calculation of  $S_{ns}$ , odd nuclei have been assumed to be spherical, which leads to a systematic overestimation of theoretical values. In the case of deformed nuclei, one observes that  $S_{ns}$  usually are overestimated, while  $S_{2n}$ s often are underestimated with the present spherical approach.

Calculations of proton and neutron density distributions have been performed for the nineteen halo nuclei using the HF and HFB procedures with the Gogny interaction. For the purpose of comparison, similar results have been derived also with the SLy4 parametrization [8] of the Skyrme force [13] using the HF method.

The proton and neutron density distributions  $\rho_{n(p)}$  for  $^{58}\text{Ni}$  are presented in Fig. 7. The Skyrme interaction gives proton and neutron densities lower by  $\simeq 10\%$  in the nucleus interior and, consequently slightly larger proton and neutron radii than the Gogny force. However, the tails of the densities obtained within the two approaches do not differ significantly from each other. Let us recall here that the parameters of the Gogny force have been determined in order to allow for the inclusion of ground state correlations in the description of one-body observables. As a consequence, nuclear radii are expected to be accurately reproduced by the Gogny force only when correlations beyond the mean-field are included.

The difference between the proton and the neutron distributions at large distance is important for the investigation of halo effects. In order to illustrate the detailed structure of these distributions, several functions of the densities  $\rho_{n(p)}$  which enter halo factors (see Section 4) have been plotted. A complete set of such results is displayed in Fig. 8 for

$^{160}\text{Gd}$  as an example. Similar plots for the remaining eighteen nuclei are shown in the next eight figures.

The upper part of Fig. 8 represents the density distributions for protons (solid lines) and neutrons (dashed lines) obtained with the Gogny force without pairing correlations (GoHF), with pairing correlations included (GoHFB) and with the Skyrme force SLy4 (SkHF) without pairing correlations. The densities are plotted up to  $r = 12$  fm, a radial distance above which they are lower than  $10^{-10}$  fm $^{-3}$ . The middle row shows the logarithms of these densities, and the leftmost diagram of the lowest row the difference  $\log \rho_n - \log \rho_p$ .

One can see that the densities computed with and without pairing correlations are very close to each other, although the contribution of pairing to the binding energy is of the order of 10 MeV.

More significant differences can be noticed between the results obtained with the SLy4 and the Gogny forces (both without pairing), especially for large  $r$  and near  $r = 0$ .

It is interesting to analyze how the different single-particle states contribute to the total density  $\rho$ . Denoting by  $\rho_\nu$  the contribution of single-particle state  $\nu$  :

$$\rho = \sum_\nu \rho_\nu \quad (4)$$

the relative contributions  $\rho_\nu/\rho$  of the occupied single-particle orbits are plotted in the rightmost diagram of the lowest row in Fig. 8. These results have been obtained from HF calculations with the Gogny force. One observes that all single particle states except one, contribute more or less the same amount in the whole region  $r = 0 - 12$  fm. At large distance and for  $r \simeq 0$ , the  $f_{7/2}$  one-neutron state strongly dominates all the other ones. This clearly indicates that the halo is a single particle effect in this nucleus, which confirms earlier results obtained with Skyrme forces [1] and with the relativistic mean field theory [3].

The middle plot of the lowest row in Fig. 8 shows the function  $(\rho_n - \rho_p) \cdot r^2/(N - Z)$  calculated within the three approaches GoHFB (solid line), GoHF (dashed line), and SkHF (dotted line). This function is strongly correlated with the magnitude of halo factors.

Similar results for the other eighteen halo nuclei listed in Table 1 are shown in the next eight figures: 9a, 9b, 10a, 10b, 11a, 11b, 12a, and 12b. Figures "a" correspond to the lighter Ca-Sn nuclei and figures "b" to the heavier Sn-U. Every multiplot presents the same quantity versus  $r$  for nine different nuclei.

In Fig. 9, the differences  $\log \rho_n - \log \rho_p$  between the logarithms of the neutron and proton densities are shown. The solid lines have been obtained with the Gogny force (GoHF), and the dashed ones with the SLy4 (SkHF) interaction. The difference between the proton and neutron densities grows with  $r$  and is larger for the Skyrme force in lighter nuclei (9a) while, for the heavier ones (9b), the Gogny force gives similar or larger density differences than SLy4.

Fig. 10 shows the contributions  $\rho_\nu$  of neutron (solid lines) and proton (dashed lines) occupied single particle orbitals  $\nu$  to the whole density  $\rho$ . One can see that in most cases

only one neutron state determines the magnitude of the density tail. For lighter nuclei (10a), only  $^{116}\text{Cd}$  and  $^{100}\text{Mo}$  have more than one neutron state contributing to the tail of the density. In heavier nuclei, Fig. 10b, the Sn and Te isotopes show a similar behaviour, with two neutron orbitals contributing to the density tail. A very interesting situation is found in  $^{144}\text{Sm}$  where the contribution that dominates corresponds to a proton state. Therefore a proton halo can be expected in this nucleus. This is in line with experimental data [1]. Unfortunately this is not the case for  $^{106}\text{Cd}$ , which also has a proton-rich nuclear stratosphere. For every plot in Fig. 10, the quantum numbers  $lj$  of the orbital for which the contribution  $\rho_\nu$  is maximum at large distance is indicated. The single particle character of the nuclear periphery has also been found in HF calculations with the Skyrme force SkIII [1] and within the relativistic mean field theory [3].

The two Fig. 11a,b show the function  $(\rho_n - \rho_p)r^2/(N - Z)$  versus  $r$ , for the eighteen halo nuclei. This quantity directly enters the integral for the halo factor, Eq. (6), and determines the neutron or proton halo in the nuclear periphery. HF results are shown both for the Gogny (solid line) and the SLy4 (dashed line) forces. It is apparent on these curves that the Skyrme force yields a slightly larger neutron halo than the Gogny interaction.

Figs. 12a and 12b illustrate the nuclear skin effect. The  $r^2$ -weighted difference between the average neutron  $(\rho_n/N)$  and proton  $(\rho_p/Z)$  single particle densities calculated with the Gogny force is plotted for each nucleus as a functions of  $r$ . One can see that this quantity strongly oscillates in the surface region, with variations that significantly differ in amplitude and shape, depending on the nucleus considered.

## 4 Halo factor

In experiments probing the nuclear periphery using the formation of antiproton atoms, antiprotons are caught on hydrogen-like atomic orbitals and then annihilated on the outer tail of the proton or neutron density. The halo factor is defined as [1] :

$$f \simeq \frac{Z \sum_s \Gamma_n^s}{N \sum_s \Gamma_p^s}, \quad (5)$$

where the summation goes over all the antiprotonic states with meaningful annihilation widths  $\Gamma_{n(p)}^s$  on proton ( $p$ ) or neutron ( $n$ ) and  $s$  denotes the atomic state of the antiproton.

The widths are calculated by integrating the density of one kind of nucleon with the square of the antiproton wave-function  $\psi^s(r)$  :

$$\Gamma_{n(p)}^s = \int \rho_{n(p)} |\psi_{n(p)}^s(r)|^2 P(r) r^2 dr. \quad (6)$$

$\psi^s(r)$  is taken as the solution of the Schrödinger equation for a hydrogen-like antiprotonic atom. The nucleus is assumed to be spherical. Let us point out that the nuclear radius is much smaller than typical antiproton orbital radii.

The factor  $P(r)$  describes the probability that the annihilation products of the antiproton will not be absorbed by the nucleus. This factor, which should depend on the atomic state of the antiproton, will be assumed here to be independent of it.  $P(r)$  takes into account the deep hole creation probability  $P_{\text{dh}}(r)$  and the pion escaping probability  $P_{\pi,\text{esc}}(r)$ . For the ground state nuclear periphery, only cold annihilation is important. Hot annihilation has to be eliminated from the widths  $\Gamma$ , which leads to the  $P(r) = \text{constant}$  approximation.

In Fig. 13 the halo factors obtained with the Gogny and Skyrme forces are compared with the experimental data taken from Ref. [1]. The variations of experimental halo factors from nucleus to nucleus are satisfactorily reproduced by the two theoretical calculations. In most cases, the Gogny force gives smaller halo factors than the Skyrme interaction, which is consistent with the fact that the Gogny D1S parameterization underestimates radii when correlations beyond the mean field are neglected. This is especially true in the five heavier nuclei which all are deformed. The halo factors derived with SLy4 appear in good quantitative agreement with experimental data. In particular, the unusually large halo factor in  $^{176}\text{Yb}$  is well reproduced. Let us note that both effective interactions significantly underestimate the halo factors of the two Te isotopes, which indicates that the halo structure of these two spherical nuclei is not properly described by the present microscopic calculations. One reason for these discrepancies may be that correlations beyond the mean-field approximation are necessary for a correct description of neutron densities at large distance in these nuclei.

## 5 Conclusions

Hartree–Fock–Bogoliubov calculation in spherical symmetry have been performed with the Gogny force for nineteen halo nuclei. The parameters of the HO bases employed – maximum number of shells  $N_{\text{MAX}}$  and frequency  $\hbar\omega$  – have been carefully chosen in order to ensure the convergence of the total binding energy, and to describe the large distance behaviour of nucleon density distributions.

The following conclusions can be drawn from the present investigation:

1. One- and two- neutron separation energies are reproduced with the Gogny force within  $\pm 1$  MeV in most of the spherical nuclei studied. In deformed nuclei, the spherical symmetry assumption leads to an underestimation of  $S_{2ns}$  and an overestimation of  $S_{ns}$  that can reach 3 MeV.
2. The Gogny force D1S gives an overall satisfactory account of the nuclear periphery which could probably be improved by taking into account deformation effects and, to a lesser extent, correlations beyond the mean field. Inclusion of pairing correlations in the self-consistent calculation induces only weak changes in the proton and neutron density distributions, and has a negligible effect on halo factors.
3. The variations of halo factors from nucleus to nucleus obtained with the Gogny force and the SLy4 interaction are in good agreement with experimental data. From the

present spherical mean-field calculations, SLy4 gives a larger neutron halo effect than the Gogny force, in better agreement with experiments.

As almost half of experimentally known halo–nuclei are well deformed, a test of the influence of including nuclear deformation in the self-consistent calculations is clearly needed. In the case of the Gogny force, a similar test concerning the effect of the ground state correlations associated with oscillations of the mean-field – large amplitude collective motion in soft nuclei, RPA ground state correlations in rigid nuclei – and of possible shape coexistence phenomena should also be performed. This is left for future work.

## References

- [1] P. Lubiński, J. Jastrzębski, A. Trzcińska, W. Kurcewicz, H. J. Hartman, W. Schmid, T. von Egidy, R. Smolańczuk, S. Wycech, Phys. Rev. **C57** (1998) 2962.
- [2] S. Wycech, F. J. Hartmann, H. Damel, W. Kanert, H. S. Pleudl, T. von Egidy, J. I. Reidy, M. Nicholas, L. A. Redmond, H. Koch, A. Kreissl, H. Path, D. Redmann, Nucl. Phys. **A561** (1993) 607.
- [3] A. Baran, K. Pomorski, M. Warda, Z. Phys. **A357** (1995) 33.
- [4] J. Dechargé, D. Gogny, Phys. Rev. **C21** (1980) 1568.
- [5] A. Baran, L. Egido, B. Nerlo-Pomorska, K. Pomorski, P. Ring, L. M. Robledo, J. Phys. **G21** (1995) 854.
- [6] M. Girod, P.G. Reinhard, Nucl. Phys. **A384** (1982) 179.
- [7] J. F. Berger, M. Girod, D. Gogny, Nucl. Phys. **A428** (1984) 236.
- [8] E. Chabanat, P. Bonche, P. Haensel, J. Meyer, R. Schaefer, Nucl. Phys. **A625** (1997) 710.
- [9] D. Gogny, in Proc. Int. Conf. on "Nuclear Physics with Electromagnetic Interactions", Mainz (Germany), 1979.
- [10] M. Girod and D. Gogny, Phys. Lett. B **64** (1976) 5.
- [11] J. M. Pearson et al., Nucl. Phys. **A459** (1992) 155.
- [12] G. Audi, A. H. Wapstra, Nucl. Phys. **A595** (1995) 409.
- [13] T. H. R. Skyrme, Nucl. Phys. **9** (1959) 615.

## Table captions:

1. The results of the Hartree-Fock-Bogoliubov calculation with the Gogny D1S force for 19 halo nuclei [1]. The harmonic oscillator basis parameters: the shell number  $N_{MAX}$  and the oscillator frequency  $\hbar\omega$ , the binding energies  $B$ , one  $S_n$  and two  $S_{2n}$  neutron separation energies, the equilibrium deformation  $\beta_2$  and the theoretical  $f$  and experimental halo factors are listed in the table.

## Figure captions:

1. Hartree-Fock energy (crosses) obtained with the Gogny force in  $^{58}\text{Ni}$  versus the frequency ( $\hbar\omega$ ) of the harmonic oscillator basis. The theoretical points are interpolated by 2<sup>nd</sup> order polynomial in  $\hbar\omega$ .
2. Hartree-Fock energy (crosses) obtained with the Gogny force in  $^{58}\text{Ni}$  as a function of the number ( $N_{MAX}$ ) of harmonic oscillator shells included in the basis.
3. Contours of the Hartree-Fock energy (crosses) obtained with the Gogny force in  $^{58}\text{Ni}$  in the ( $N_{MAX}$ ,  $\hbar\omega$ ) plane.  $N_{MAX}$  is the number of shells included in the harmonic oscillator basis and  $\hbar\omega$  is the harmonic oscillator frequency.
4. Logarithms of the neutron density distribution  $\rho_n$  as functions of the radial distance  $r$  in  $^{58}\text{Ni}$ . The different curves correspond to different values of the harmonic oscillator basis frequency  $\hbar\omega$ .
5. Difference between theoretical (Gogny) and experimental [12] one-neutron separation energies  $S_n$  for experimentally known halo-nuclei.
6. Same as Fig.5 for two-neutron separation energies  $S_{2n}$ .
7. Proton (dashed and dotted lines) and neutron (solid, thin dashed lines) density distributions obtained from Hartree-Fock calculations with the Gogny force (GoHF) and with the Skyrme SLy4 force (SkHF), versus the radial distance  $r$ .
8. Density distribution results obtained in  $^{160}\text{Gd}$ . First row: Density distributions for protons  $\rho_p$  (solid lines) and neutrons  $\rho_n$  (dashes lines) obtained from Hartree-Fock calculations with the Gogny force D1S (first column), from Hartree-Fock-Bogoliubov calculations with the Gogny force (second column), and from Hartree-Fock calculations with the Skyrme force SLy4 (third column). Second row: Logarithms  $\log \rho_{n(p)}$  of the densities shown in the first row. Third row, first column: the difference  $\log \rho_n - \log \rho_p$  between the logarithms of the neutron and proton densities; second column: the function  $(\rho_n - \rho_p)r^2/(N - Z)$  obtained by applying the Hartree-Fock method with the Gogny force D1S (GoHF, dashed line), the Hartree-Fock-Bogoliubov method with the Gogny force (GoHFB, solid line) and the Hartree-Fock

method with the Skyrme force SLy4 (SkHF, dotted line); third column: single-particle contributions  $\rho_\nu$  to the density  $\rho$  for protons (solid lines) and neutrons (dashed lines). The  $l_j$  quantum numbers of the orbit with largest  $\rho_\nu$  at  $r = 12$  fm are indicated in each plot.

- 9a. The differences  $\log \rho_n - \log \rho_p$  obtained from Hartree-Fock calculations with the Gogny force D1S (GoHF – solid lines), and with the Skyrme force SLy4 (SkHF – dashed lines) for the nine lighter halo-nuclei  $^{48}\text{Ca}$  to  $^{112}\text{Sn}$ .
- 9b. Same as Fig. 9a for the nine heavier halo-nuclei  $^{124}\text{Sn}$  to  $^{238}\text{U}$ .
- 10a. Relative contributions  $\rho_\nu/\rho$  of the single particle proton (dashed lines) and neutron (solid lines) states  $\nu$  to the total density  $\rho$  as functions of the radial distance  $r$  for the nine lighter halo-nuclei  $^{48}\text{Ca}$  to  $^{112}\text{Sn}$ .
- 10b. Same as Fig. 10a for the nine heavier halo-nuclei  $^{124}\text{Sn}$  to  $^{238}\text{U}$ .
- 11a. The function  $(\rho_n - \rho_p)r^2/(N - Z)$  obtained from Hartree-Fock calculations with the Gogny force D1S (solid lines), and with the Skyrme force SLy4 (dashed lines) versus the radial distance  $r$  for the nine lighter halo-nuclei  $^{48}\text{Ca}$  to  $^{112}\text{Sn}$ .
- 11b. Same as Fig. 11a for the nine heavier halo-nuclei  $^{124}\text{Sn}$  to  $^{238}\text{U}$ .
- 12a. The function  $(\rho_n/N - \rho_p/Z)r^2$  obtained from Hartree-Fock-Bogoliubov calculations with the Gogny force for the nine lighter halo-nuclei  $^{48}\text{Ca}$  to  $^{112}\text{Sn}$ .
- 12b. Same as Fig 12a for the nine heavier halo-nuclei  $^{124}\text{Sn}$  to  $^{238}\text{U}$ .
- 13. The halo factors of experimentally known halo-nuclei obtained from Hartree-Fock-Bogoliubov calculations with the Gogny force D1S (stars joined by the thin dashed lines) and from Hartree-Fock calculations with the Skyrme forces SLy4 (crosses joined by dashed lines), compared with experimental data (plusses with errorbars joined by solid lines) from Ref. [1].

Table 1

Nucleus	N <sub>MAX</sub>	$\hbar\omega$	B	$S_n$	$S_{2n}$	$\beta_2$ [11]	f	$f_{\text{exp}}$ [1]
–	–	MeV	MeV	MeV	MeV	–	–	–
<sup>48</sup> Ca	14	16.442	416.838	11.574	15.735	0	1.77	2.35±0.35
<sup>58</sup> Ni	16	15.470	505.161	11.663	21.562	0	1.10	1.30±0.2
<sup>96</sup> Zr	16	13.479	825.345	7.958	12.202	-0.19	2.04	3.7±0.6
<sup>96</sup> Ru	16	15.070	827.972	9.616	17.366	0	1.14	1.10±0.2
<sup>100</sup> Mo	18	12.962	856.871	8.070	12.980	-0.27	2.53	4.10
<sup>104</sup> Ru	18	14.256	888.612	9.233	14.001	-0.28	2.24	4.30
<sup>106</sup> Cd	16	14.254	903.668	10.688	18.138	0	1.38	0.60±0.1
<sup>112</sup> Sn	16	14.212	952.850	10.962	18.438	0	1.56	
<sup>116</sup> Cd	16	13.761	984.182	8.861	14.793	-0.28	2.29	
<sup>124</sup> Sn	16	13.261	1049.635	9.113	14.683	0	2.47	
<sup>128</sup> Te	16	13.558	1078.166	9.643	15.568	0	2.02	4.3±1.1
<sup>130</sup> Te	16	13.205	1094.724	11.008	16.558	0	2.32	4.2±0.4
<sup>144</sup> Sm	18	14.141	1197.497	12.838	20.981	0	2.55	<0.5
<sup>148</sup> Nd	16	11.898	1216.816	8.458	9.831	0.23	2.40	4.8±0.9
<sup>154</sup> Sm	18	12.351	1253.112	8.674	10.659	0.28	2.56	2.2±0.4
<sup>160</sup> Gd	18	12.222	1290.583	7.406	10.816	0.31	3.27	5.8±1.9
<sup>176</sup> Yb	18	10.182	1397.546	8.999	12.423	0.31	3.77	8.0±0.6
<sup>232</sup> Th	18	9.947	1747.601	7.724	9.540	0.21	4.00	5.4±0.8
<sup>238</sup> U	18	10.227	1778.929	7.893	10.059	0.24	3.70	5.8±0.8

Fig. 1

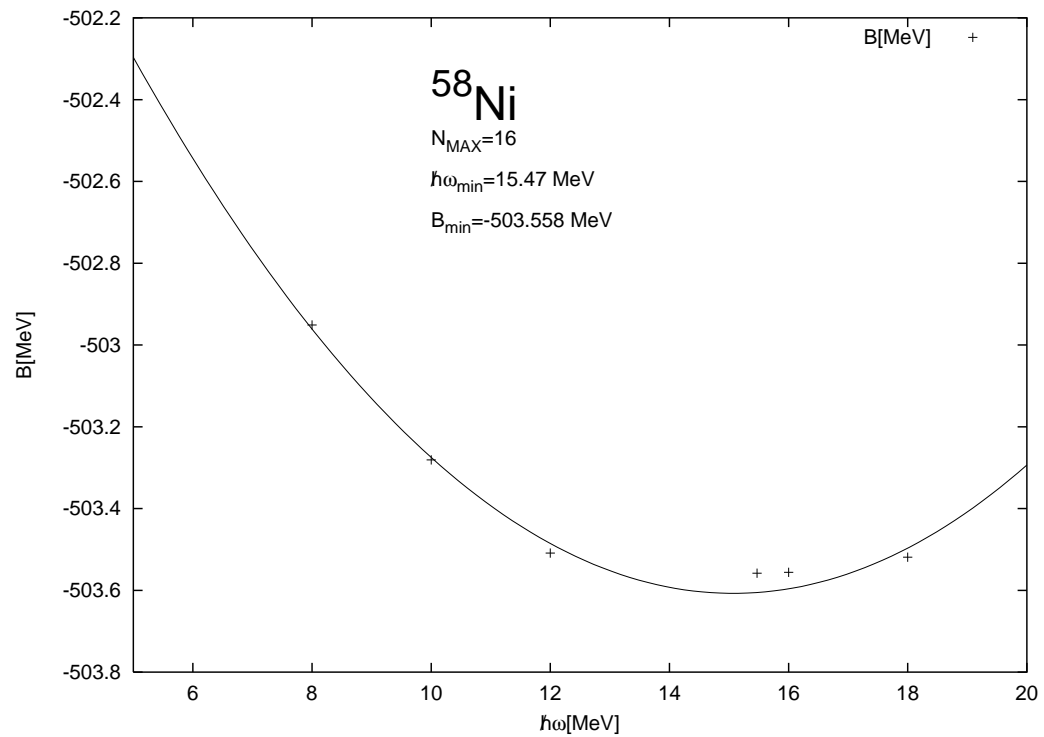


Fig. 2

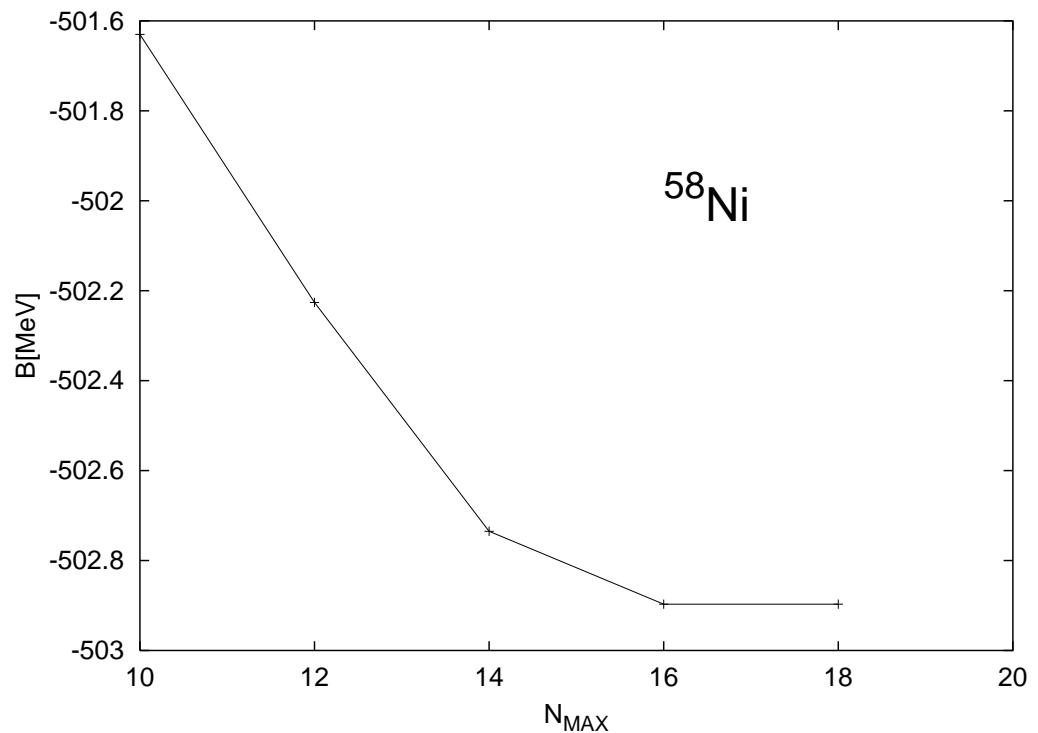


Fig. 3

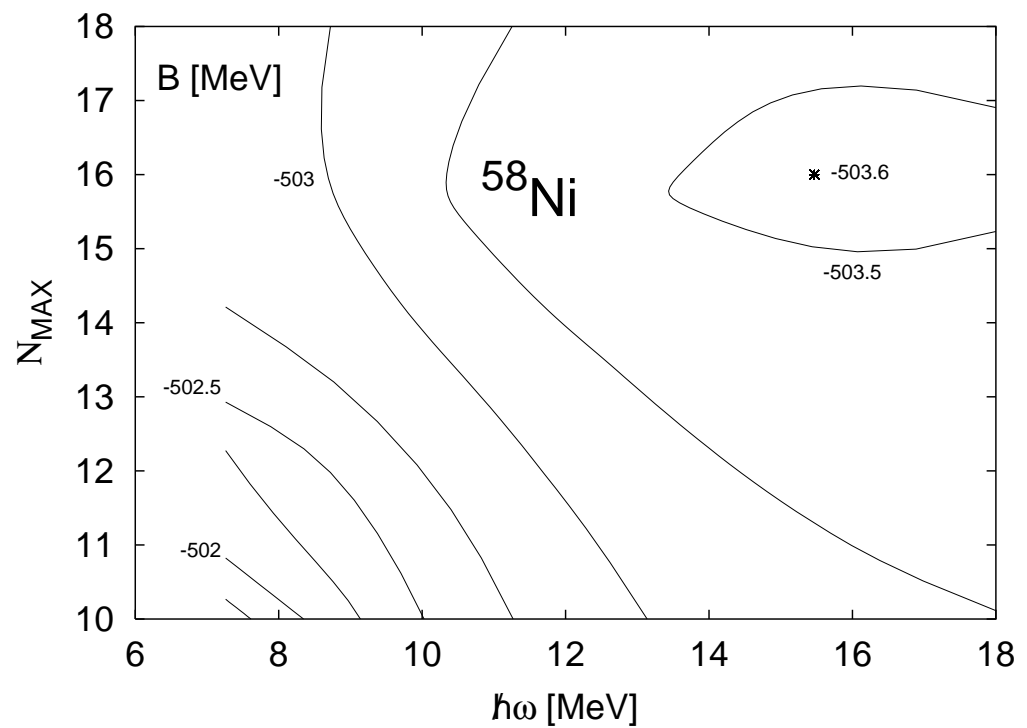


Fig. 4

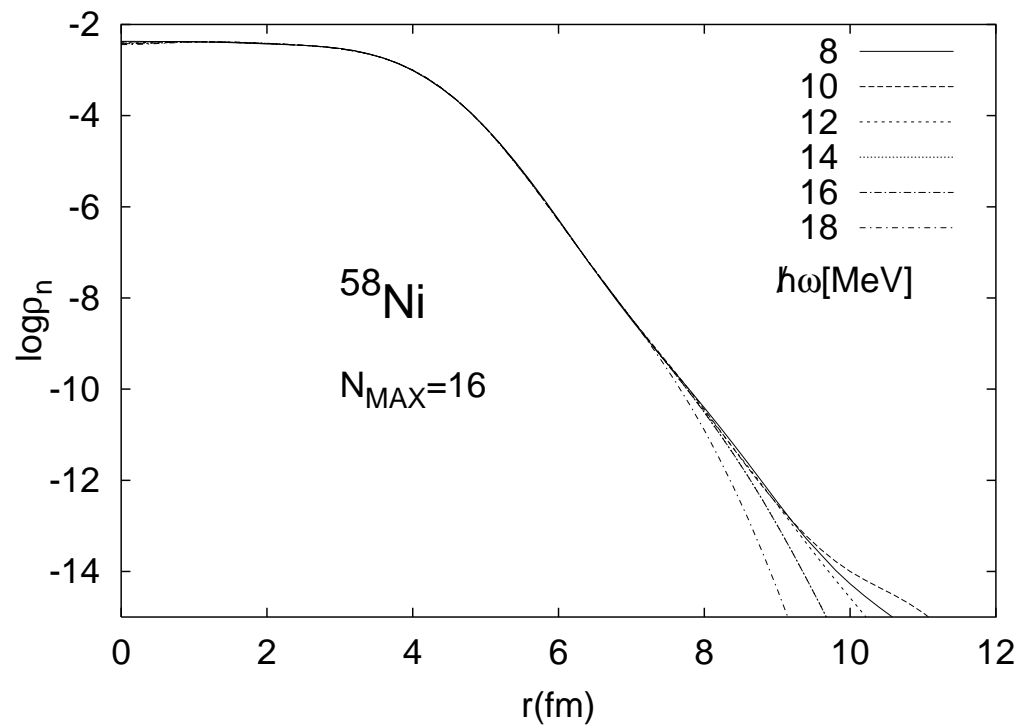


Fig. 5

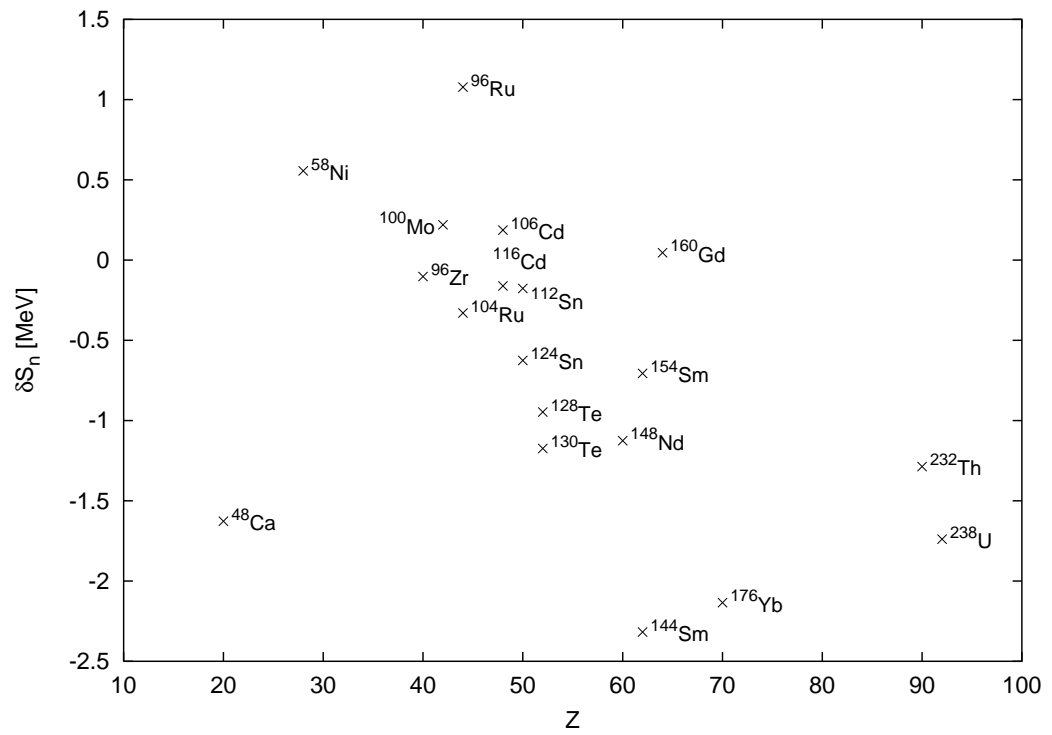


Fig. 6

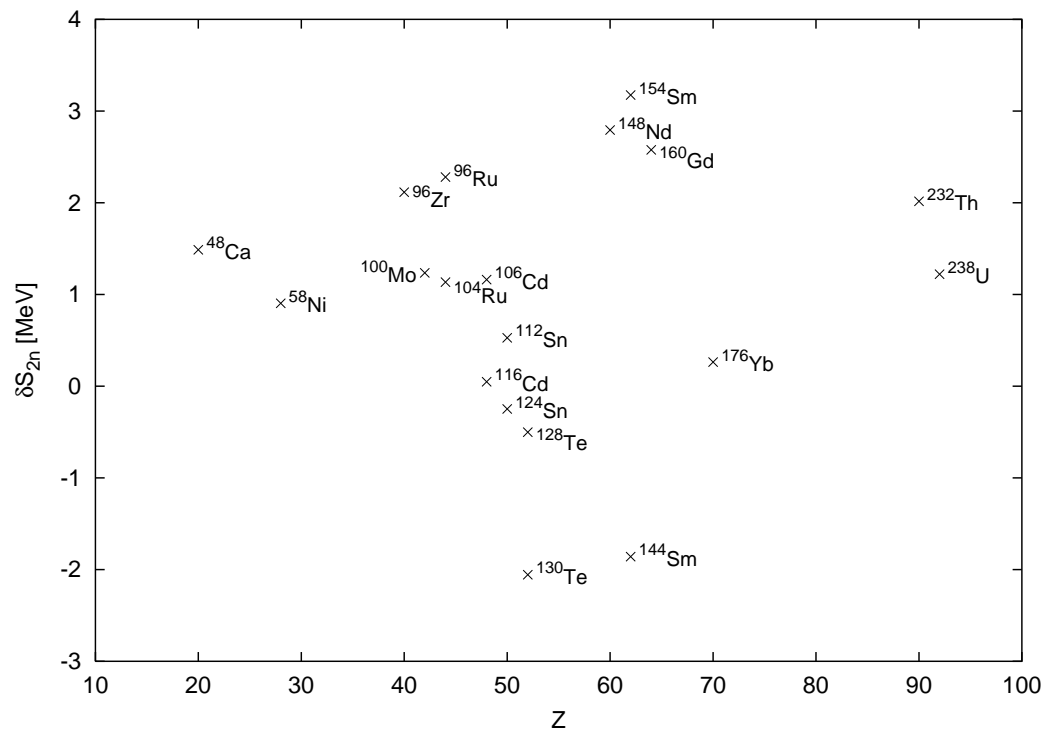


Fig. 7

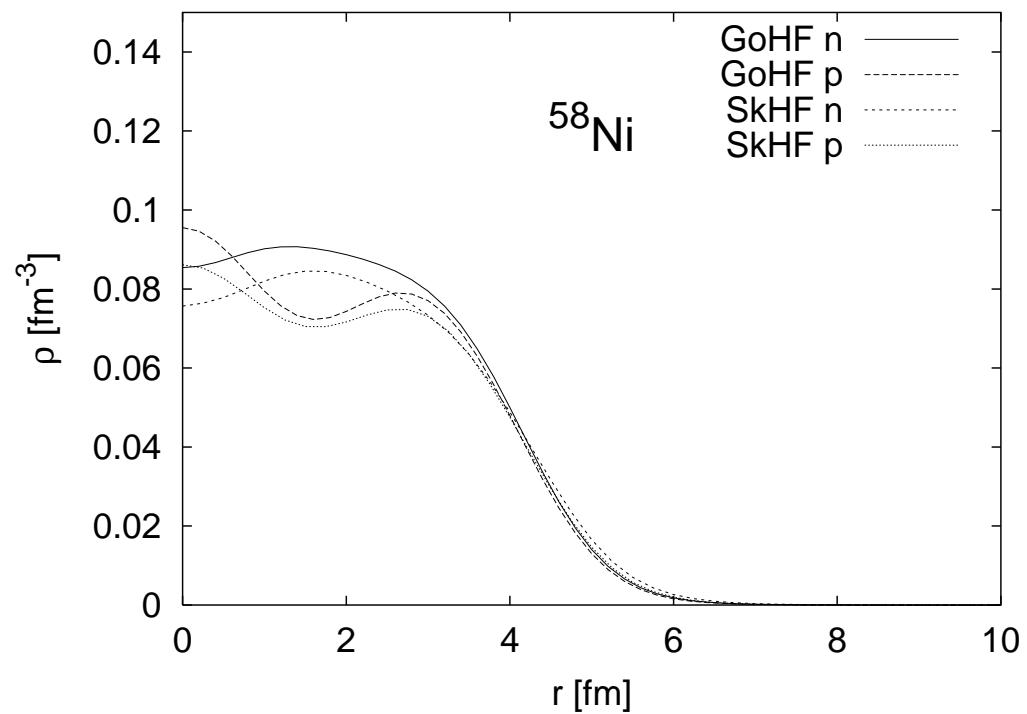


Fig. 8

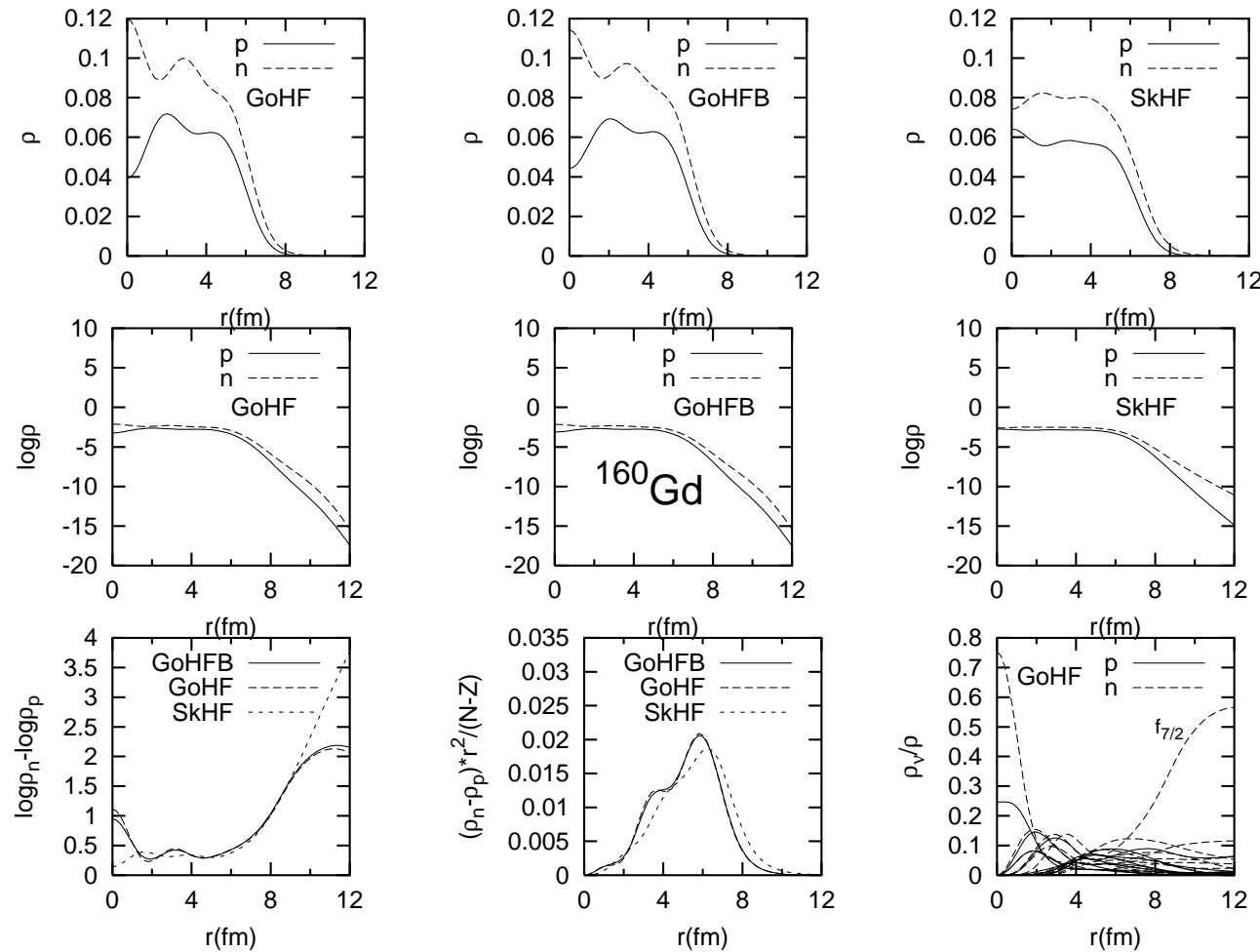


Fig. 9a

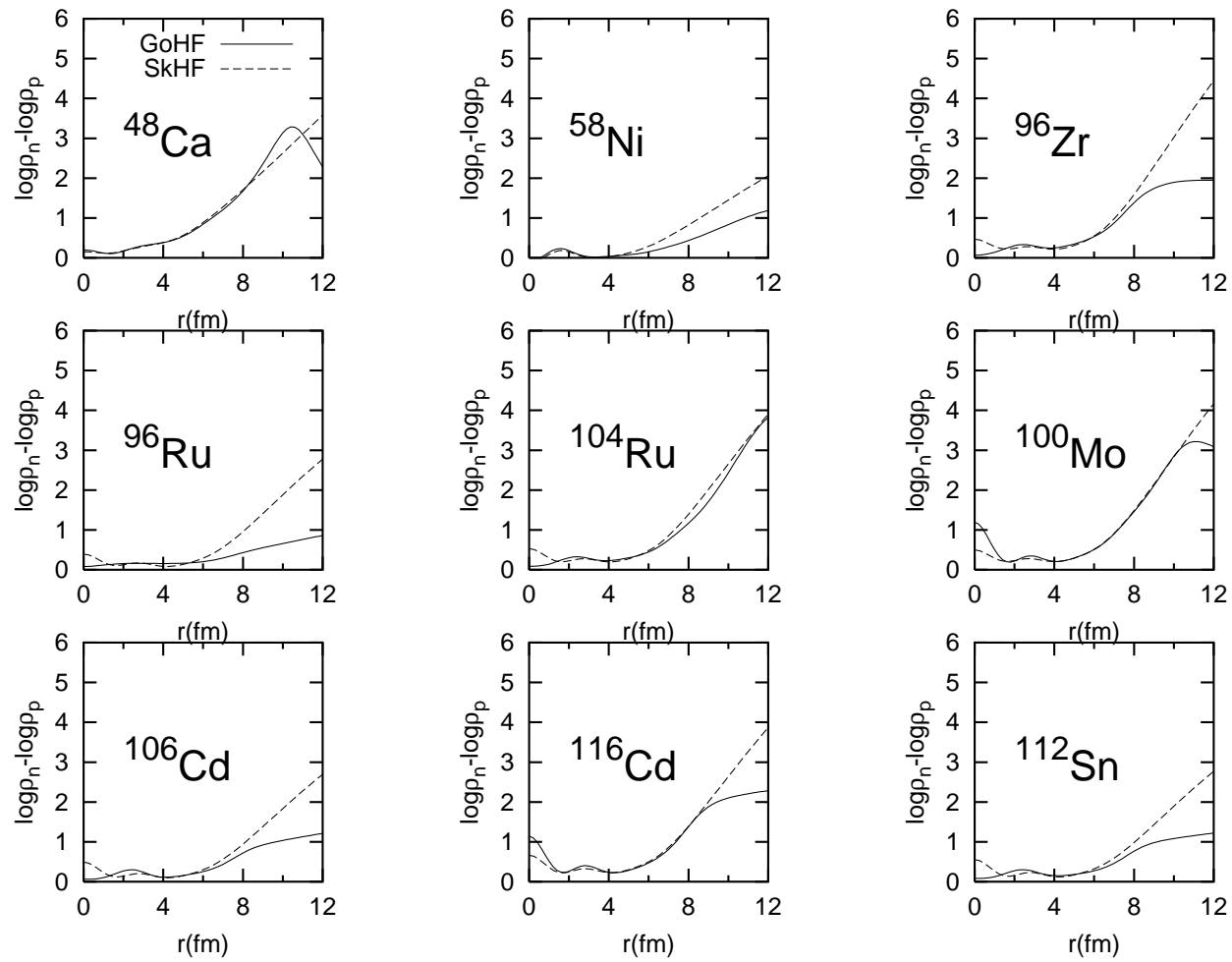


Fig. 9b

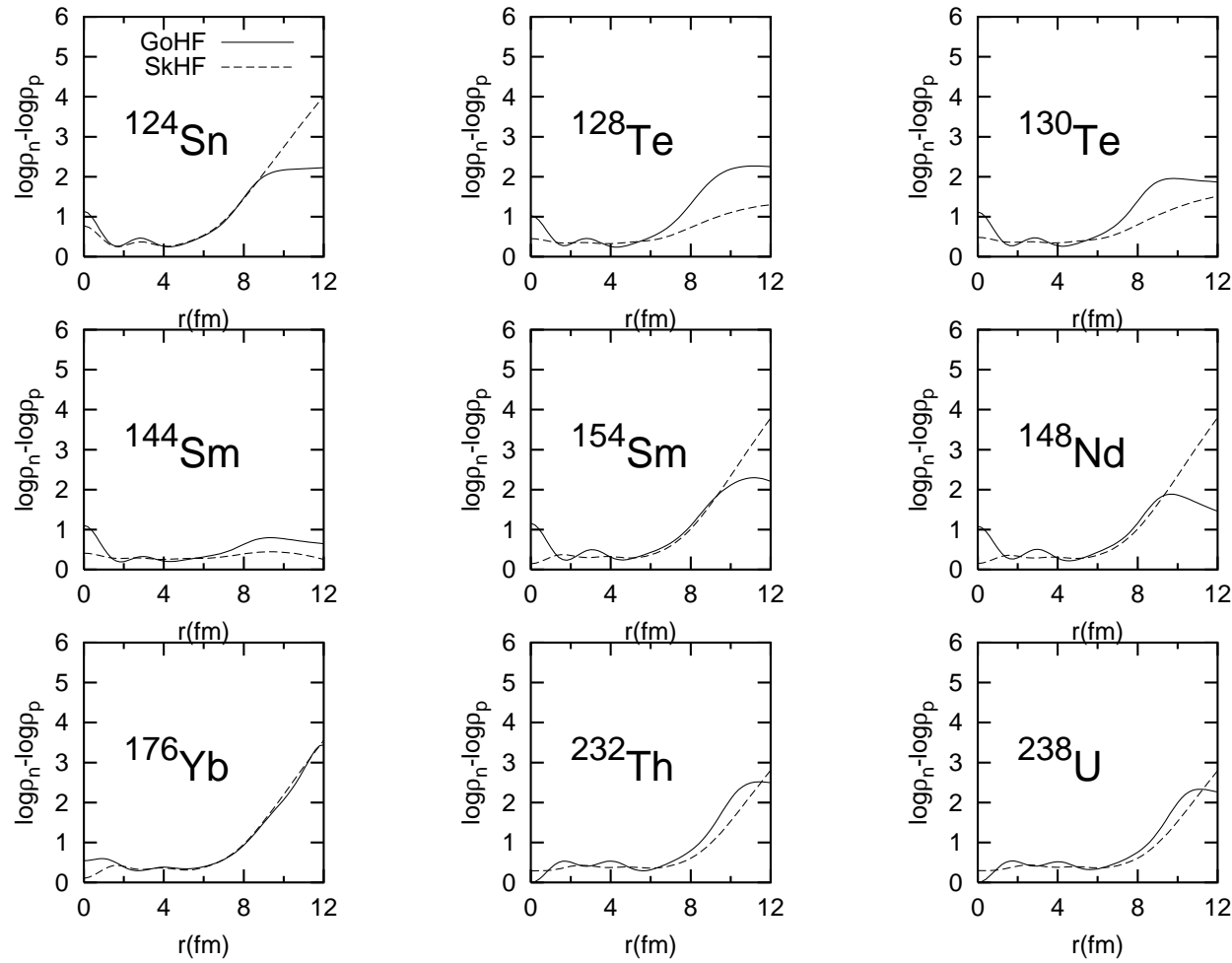


Fig. 10a

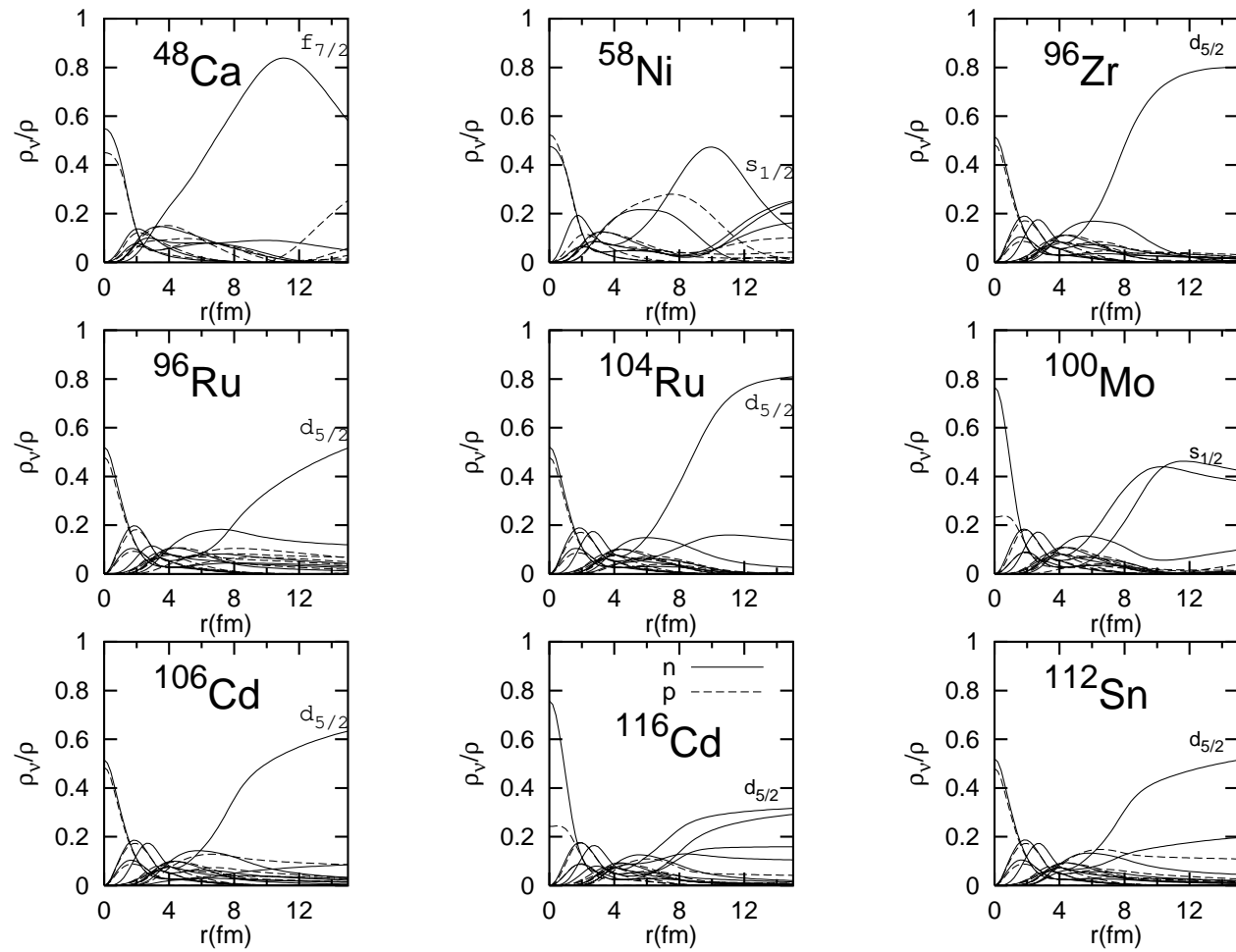


Fig. 10b

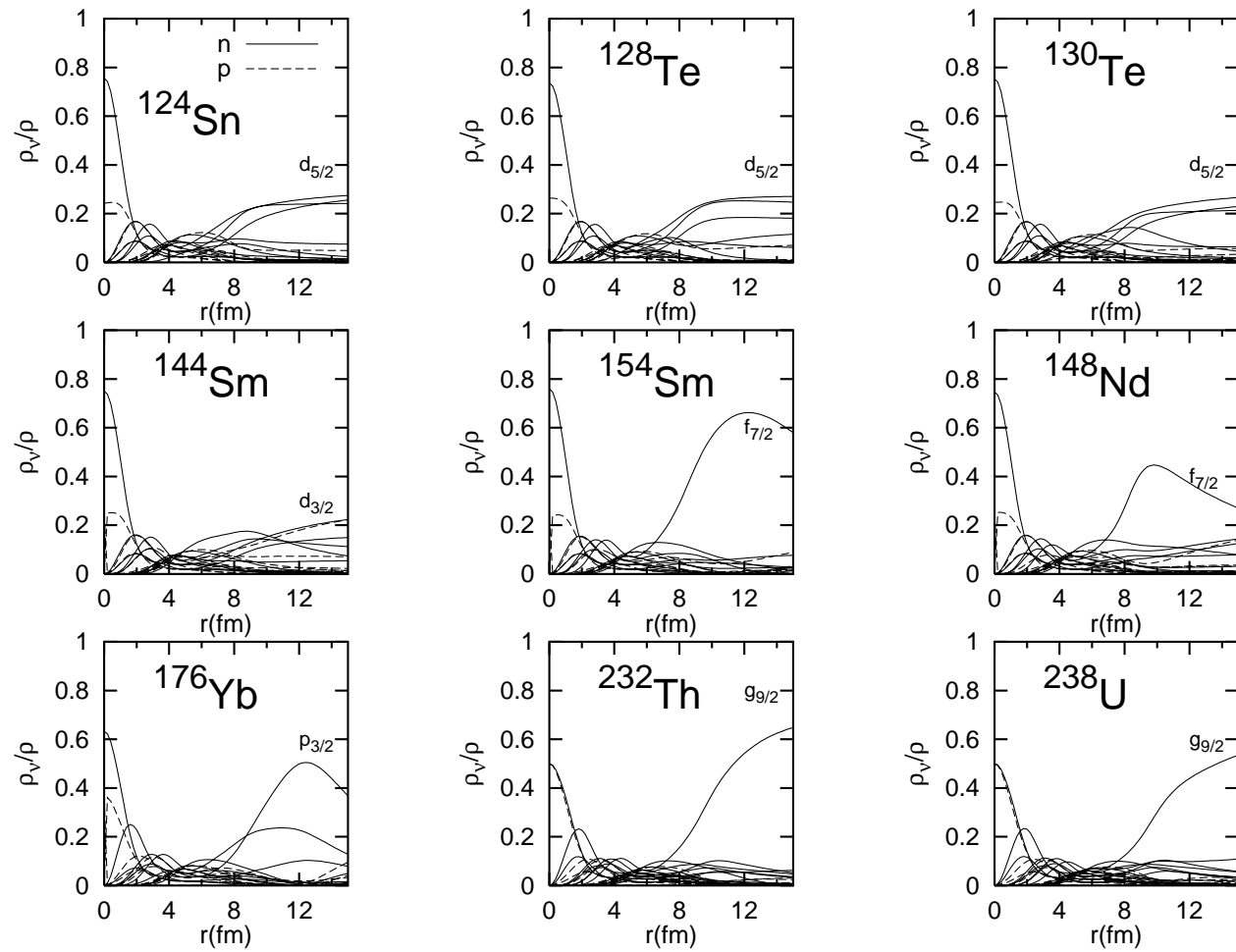


Fig. IIIa

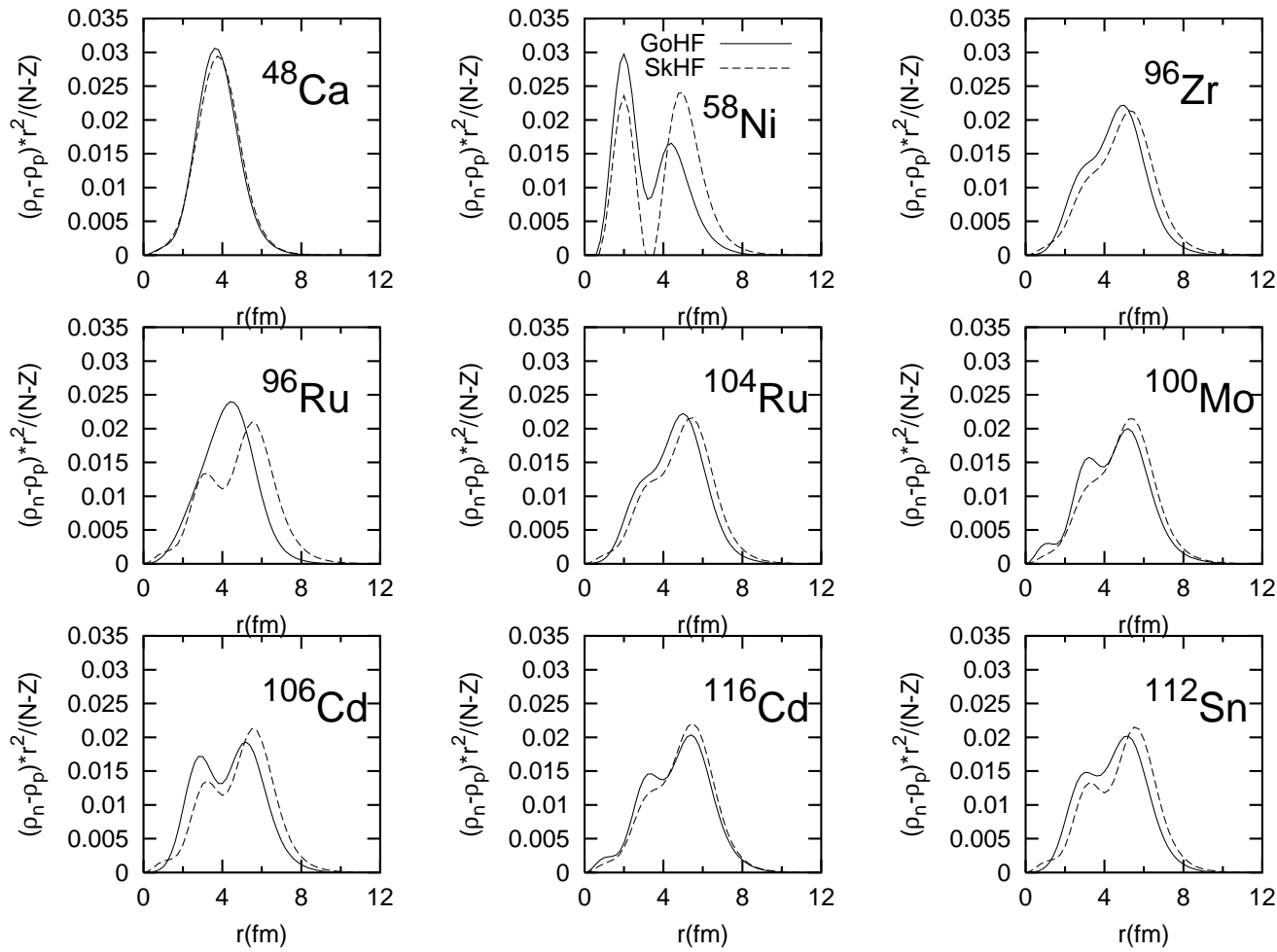


Fig. 11b

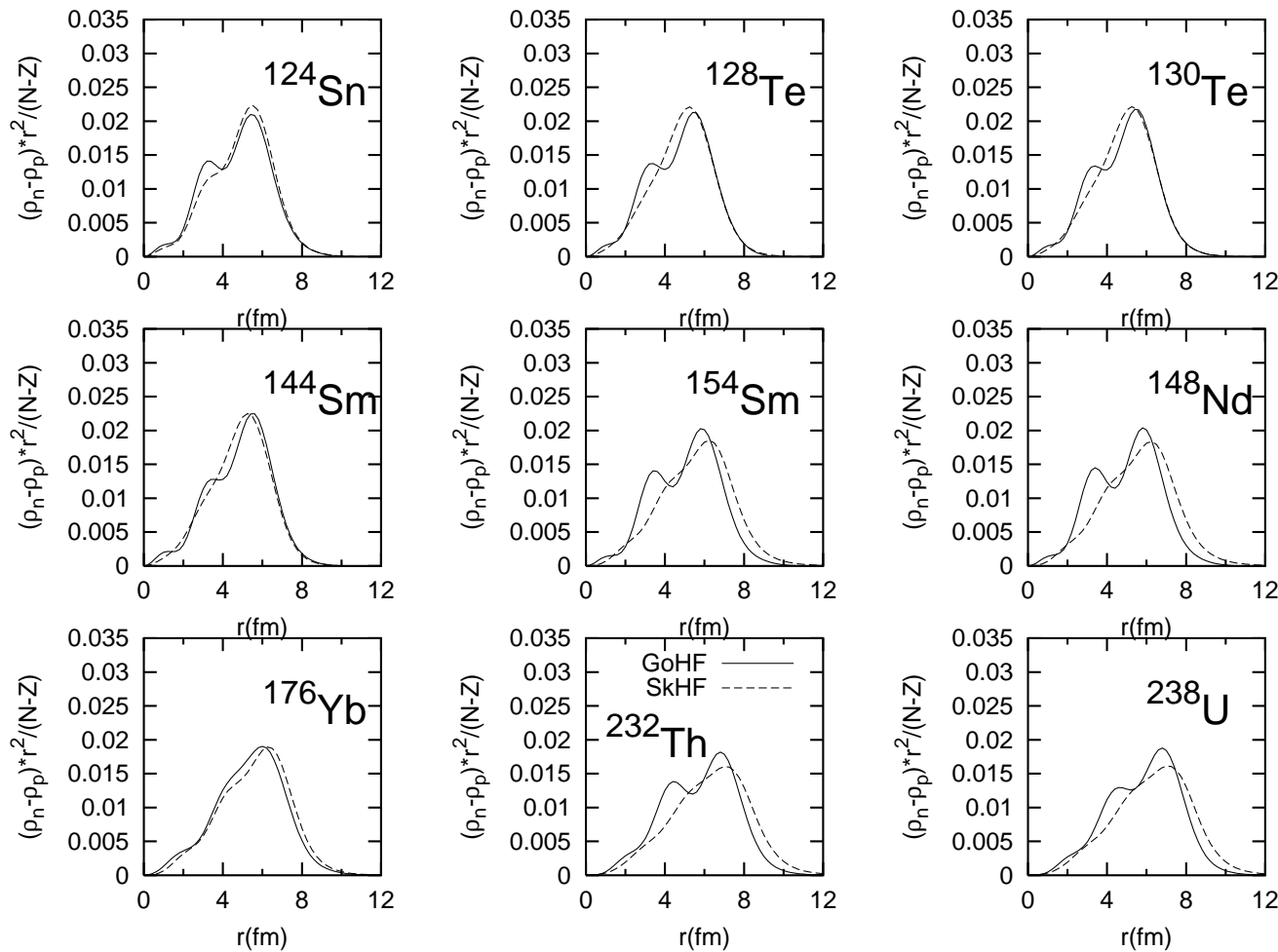


Fig. 12a

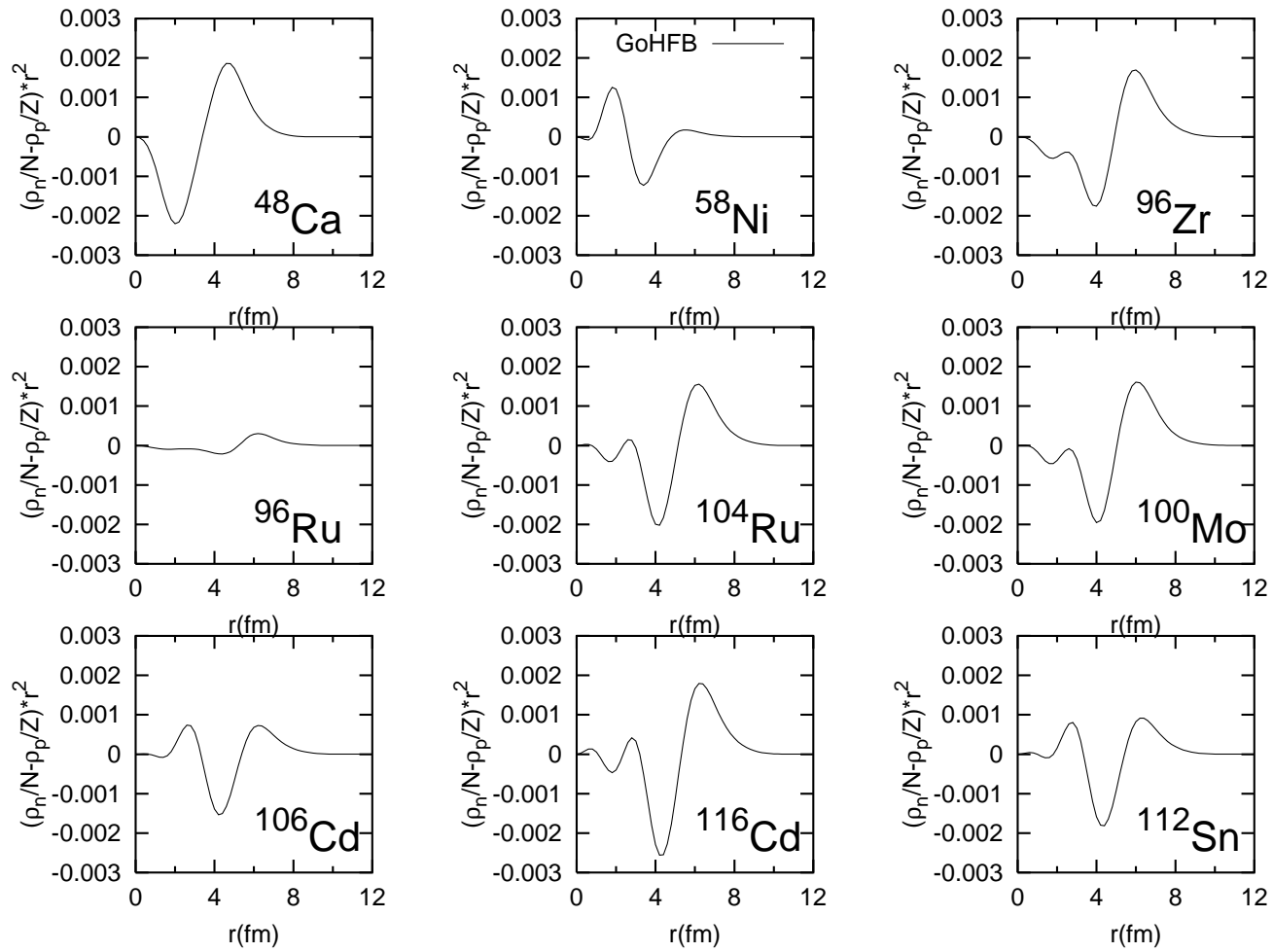
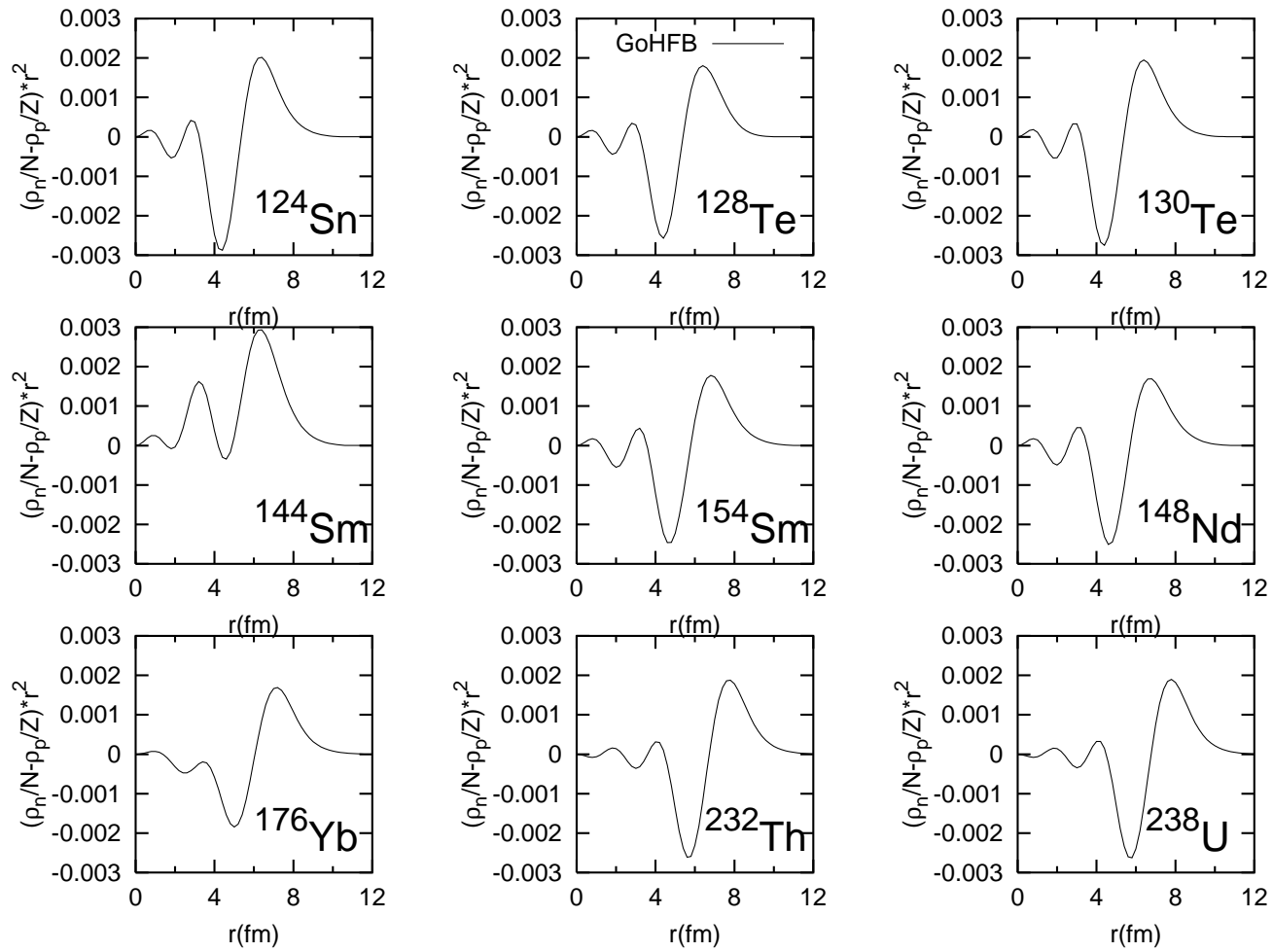


Fig. 12b



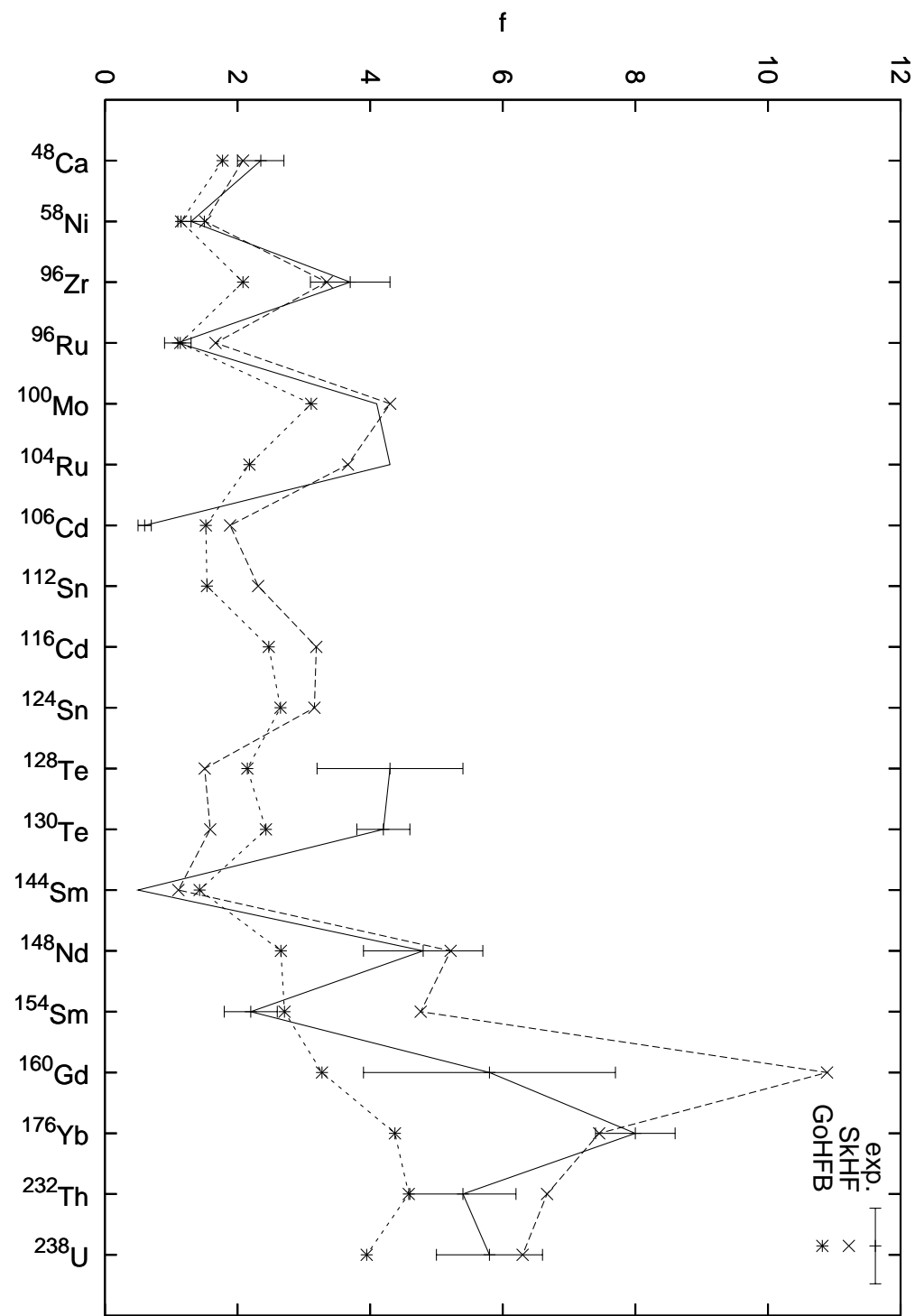


Fig. 13